

Symmetrical Turing instability in Chua corsage memristor siblings-based two-cell network

Zhicheng Tian(田柽成), Peipei Jin(靳培培), Shutong Liu(刘姝彤), Meiyuan Gu(顾梅园), Long Chen(陈龙), and Guangyi Wang(王光义)

Citation: Chin. Phys. B, 2026, 35 (**6**): 060511. DOI: 10.1088/1674-1056/ae68f9
http://cpb.iphy.ac.cn; http://iopscience.iop.org/cpb

What follows is a list of articles you may be interested in

Color image encryption algorithm using a new four-dimensional hyperchaotic system

Bo Lin(林博), Min Liu(刘敏), and Guodong Ye(叶国栋)
Chin. Phys. B, 2026, 35 (**5**): 050502. DOI: 10.1088/1674-1056/ae0bff

Impact of altruistic preference on the dynamic decision and coordination of joint emission reduction in low-carbon supply chain

Jinchai Lin(林金钗), Chunyan Zheng(郑春艳), Ruguo Fan(范如国), Yuanyuan Wang(王圆缘), Yingqing Zhang(张应青), and Han Song(宋寒)
Chin. Phys. B, 2026, 35 (**4**): 040501. DOI: 10.1088/1674-1056/ae0015

Spiking-bursting alternating chaos mediated by a locally active memristor

Yuxia Li(李玉霞), Xintong Yue(岳新同), Hui Chang(常辉), Baoxing Han(韩宝兴), and Yan Zhang(张燕)
Chin. Phys. B, 2026, 35 (**3**): 030504. DOI: 10.1088/1674-1056/ae44f9

An epidemiological stochastic predator-prey model with prey refuge and harvesting

Israr Ali, Hui Zhang(张慧), Syed Murad Ali Shah, Abdulwasea Alkhazzan, and Yassine Sabbar
Chin. Phys. B, 2026, 35 (**2**): 020503. DOI: 10.1088/1674-1056/adf17f

Nonlinear dynamics in non-volatile locally-active memristor for periodic and chaotic oscillations

Wen-Yu Gu(谷文玉), Guang-Yi Wang(王光义), Yu-Jiao Dong(董玉姣), and Jia-Jie Ying(应佳捷)
Chin. Phys. B, 2020, 29 (**11**): 110503. DOI: 10.1088/1674-1056/ab9ded

---

SPECIAL TOPIC — Biophysical circuits: Modeling & applications in neuroscience

Symmetrical Turing instability in Chua corsage memristor siblings-based two-cell network

Zhicheng Tian(田柽成), Peipei Jin(靳培培)†, Shutong Liu(刘姝彤), Meiyuan Gu(顾梅园), Long Chen(陈龙), and Guangyi Wang(王光义)

Institute of Modern Circuit and Intelligent Information, Hangzhou Dianzi University, Hangzhou 310018, *China*

(Received 16 February 2026; revised manuscript received 3 April 2026; accepted manuscript online 6 May 2026)

The Turing instability, a counterintuitive phenomenon in which two quiescent cells lose stability when coupled through a dissipative environment, has been explained via the edge of chaos theory. While the classical Turing instability and its local form have been recently elucidated, its symmetrical form — a distinct class of symmetry-breaking phenomena wherein two identical cells, each poised at a mirror-symmetrical stable operating point, undergo destabilization and bifurcate into two distinct mirror-symmetrical stable states under opposite bias voltages — has not been reported yet. This paper introduces a current-controlled odd-symmetrical Chua corsage memristor (OS-CCM) and employs it to investigate the symmetrical Turing instability in a resistively coupled two-cell network. Coupling two identical bistable OS-CCM-based cells, each originally poised at identical mirror-symmetrical stable states, via a passive resistor destabilizes their original stability, giving rise to two distinct stable states and ultimately leading to quadristability, referring to a dynamical phenomenon with four coexisting stable states, which demonstrates the emergence of symmetrical Turing instability. The quantitative condition for the emergence of this phenomenon is analytically derived and precisely determined through eigenvalue analysis. Both numerical simulations and hardware experiments confirm the correctness of the theoretical analysis.

Keywords: Chua corsage memristor, local activity, edge of chaos destabilization, symmetrical Turing instability

PACS: 05.45.–a, 82.40.Bj, 87.19.ll

DOI: 10.1088/1674-1056/ae68f9 **CSTR:** 32038.14.CPB.ae68f9

1. Introduction

Turing instability, a hidden excitability in which two quiescent cells, stable in isolation, lose stability when coupled through a dissipative environment, has remained an enigma since first proposed by Alan Turing seven decades ago.[1] The counterintuitive phenomenon was recently explained for the first time by Ascoli *et al.*,[2] via Chua's local activity theory and edge of chaos principle.[3,4] Its local form, recently elucidated and experimentally demonstrated using two homemade memristor circuit boards, exposes a distinct destabilization phenomenon, in which two quiescent cells, each possessing two stable operating points, lose stability at one of their locally stable operating points, giving rise to a pair of new stable states.[5] This finding extends the existing form of Turing instability. The mechanisms of Turing instability provide a design principle for memristor-based neurons and neural networks,[6–8] and offer a theoretical foundation for pattern recognition and edge detection in brain-inspired computing.[9–11]

Turing instability and its dynamic patterns in higher-dimensional space, known as the Smale paradox, are symmetry-breaking phenomena produced by coupling two identical and quiescent cells with a dissipative environment.[1,12] The classical form of Turing instability and its mechanisms were recently explained in Ref. [2], in which a two-cell network was designed by employing two NaMLab NbO_x memristors endowed with edge-of-chaos domains, thereby providing the first rigorous demonstration of Turing instability in a memristive array. Its higher-dimensional form, the Smale paradox, was successfully reproduced using two memristive neurons, accompanied by the first hardware demonstration of this complex symmetry-breaking phenomenon.[13] Moreover, symmetry-breaking phenomena in high-order reaction–diffusion cellular nonlinear networks were established.[14] A comprehensive bifurcation analysis was reported in Ref. [2]. Beyond reaction–diffusion systems, symmetry-breaking phenomena have also been exploited in dynamical systems to generate asymmetric pairs of attractors, as reported in Refs. [9,15].

To extend the existing forms of Turing instability and to conduct a more rigorous investigation into its underlying mechanisms, the local form of Turing instability was proposed.[5] They designed a two-cell network comprising a pair of identical current-controlled Chua corsage memristors coupled through a passive resistor and demonstrated that destabilization of the bistable cells occurs only if each individ-

†Corresponding author. E-mail: jinpeipei@hdu.edu.cn

© 2026 Chinese Physical Society and IOP Publishing Ltd. All rights, including for text and data mining, AI training, and similar technologies, are reserved.

ual cell converges to a locally stable and locally active operating point when evolving in isolation. Also, an experimental demonstration of the local Turing instability on a physical memristive medium has first been reported. However, its symmetrical form has not yet been reported. Specifically, Turing instability is applicable for oscillatory circuit construction.[16] The mechanism of Turing instability and a related Hopf bifurcation analysis were detailed in Ref. [17].

The Chua corsage memristor (CCM), a hypothetical memristor proposed by L. Chua, is endowed with an edge-of-chaos domain, making it possible to reproduce Turing instability.[18] Importantly, a functioning homemade CCM circuit board has been built using only off-the-shelf electronic components in Refs. [19,20]. Compared to memristor devices fabricated from exotic materials and advanced nanofabrication machines, such as the NbO_2 Mott memristor[21] and the VO_2 locally active memristor,[22] the homemade CCM circuit board offers a more accessible kit for researchers and students to conduct hardware validation of Turing instability. Also, three CCM siblings, termed the odd-symmetric CCM, current-controlled CCM, and asymmetric CCM, have been introduced to facilitate the exploration of more complex phenomena.[5,23,24] In particular, the current-controlled CCM was employed to demonstrate local Turing instability.[23] The odd-symmetric CCM, featuring symmetrical edge-of-chaos domains, is capable of generating biphasic action potentials.[5] Besides, discrete corsage memristors and a discrete neuron circuit, together with their systematic dynamics analysis and circuit implementation, were reported in Refs. [25,26]. A ReLU function-based locally active memristor was reported in Ref. [27]. Locally active memristor-based multisensory memristive circuits and supramodal attention effects were presented in Refs. [28,29].

The motivation of this paper is to introduce a novel current-controlled odd-symmetric CCM, and to employ it in constructing a two-cell network for the theoretical analysis and hardware demonstration of symmetrical Turing instability, thereby extending the classical concept of Turing instability.

Finally, this paper is organized as follows. Section 2 introduces the current-controlled odd-symmetrical CCM model and analyzes its odd-symmetric local activity and edge of chaos. Section 3 presents the theoretical analysis of symmetrical Turing instability in a two-cell coupled network. Section 4 experimentally confirms the symmetric Turing instability using homemade memristor circuit boards. Section 5 concludes the paper.

2. Chua corsage memristor sibling

The first hardware demonstration of Turing instability was observed in a resistively coupled two-cell network, where each cell comprises a current-controlled Chua corsage memristor (CCM), whose equations are given as follows:

$$v_{\mathrm{M}} = R(x) i_{\mathrm{M}} = G x^2 i_{\mathrm{M}}, \tag{1a}$$

$$\frac{\mathrm{d}x}{\mathrm{d}t} = g(x, i_{\mathrm{M}}) = K(a - x + |x-b| - |x-c| + T i_{\mathrm{M}}), \tag{1b}$$

where v_{M}, i_{M} and x denote the voltage, current and state variable of the current-controlled CCM, respectively; $R(x)$ and $g(x,\ i_{\mathrm{M}})$ represent the memristance function and state equation of the memristor, where $a = 30$, $b = 20$, $c = 40$, $G = 20$, $K = 10^4$ and $T = 10^3$ are the scaling constants.

The DC V_{M}–I_{M} curves of the current-controlled CCM and their enlarged negative differential resistance (NDR) domain, the fingerprint for local activity, are reproduced in Fig. 1 for the reader's convenience.

Figure 1(a) presents the DC V_{M}–I_{M} curve of the current-controlled CCM obtained by the parameter-sweeping method,[18] which includes three branches corresponding to different state variable X (note that X is the DC operating point of the state variable x of the memristor defined by Eq. (1) and is the equilibrium point $Q = X$ of the memristor). Figure 1(b) displays the enlarged blue sub-branch, showing the only S-shaped NDR segment over the range $-3\ \mathrm{V} < V_{\mathrm{M}} < 0\ \mathrm{V}$ and $-10\ \mathrm{mA} < I_{\mathrm{M}} < -3.33\ \mathrm{mA}$. Turing instability can be observed in this NDR region, which has been demonstrated in our previous work.[5] However, this single asymmetric NDR region restricts the emergence of symmetrical Turing instability, which is essential for studying mirror-symmetrical Turing patterns.

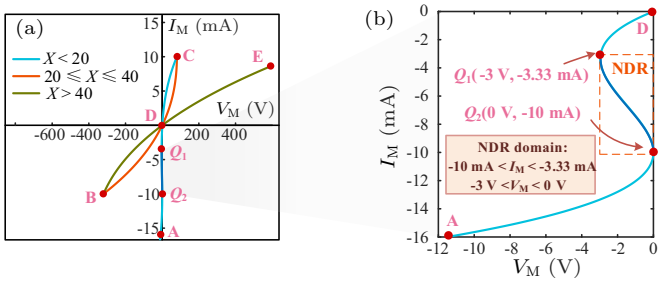


Fig. 1. (a) DC V_{M}–I_{M} characteristic of the current-controlled CCM obtained by sweeping the state variable X, showing the blue branch with $X < 20$, red branch with $20 \leq X \leq 40$ and green branch with $X > 40$. (b) Enlarged view of the blue branch in (a), highlighting the S-shaped NDR region within $-3V < V_{\mathrm{M}} < 0$ V and $-10\ \mathrm{mA} < I_{\mathrm{M}} < -3.33$ mA, enclosed within an orange dashed box bounded by points Q_1 and Q_2.

To overcome this limitation, a novel CCM sibling, a current-controlled odd-symmetrical CCM (OS-CCM), is proposed here by introducing a squared current term into the state equation of the above current-controlled CCM and adjusting the scaling constants to accommodate the operating voltage and current ranges in milliamperes (mA) and volts (V). Its equations are described by

$$v_{\mathrm{M}} = G x^2 i_{\mathrm{M}}, \tag{2a}$$

$$\frac{\mathrm{d}x}{\mathrm{d}t} = K(a - x + |x-b| - |x-c| + T i_{\mathrm{M}}^2), \tag{2b}$$

where $v_{\rm M}$ and $i_{\rm M}$ represent the voltage and current of the current-controlled OS-CCM, and x is its internal state variable. The introduction of the squared term $i_{\rm M}^2$ in the state equation ensures the odd symmetry of the current-controlled OS-CCM and enables the emergence of two symmetrical locally active domains. This symmetry of the memristor is essential for realizing symmetrical Turing instability. In Eq. (2b), $a = 30$, $b = 14$, $c = 46$, $G = 75$, $K = 10^4$, and $T = 2 \times 10^3$ are the scaling constants.

To visualize the effect of the squared current term in the state equation of the current-controlled OS-CCM, its DC $V_{\rm M}$–$I_{\rm M}$ characteristic and the corresponding enlarged NDR segments are displayed in Fig. 2.

Figure 2 displays the complete DC $V_{\rm M}$–$I_{\rm M}$ curve of the current-controlled OS-CCM over the range $X \geq -2$, and its enlarged S-shaped sub-branches, which contain NDR regions. X, $V_{\rm M}$, and $I_{\rm M}$ are the DC operating points of the state variable x, voltage $v_{\rm M}$, and current $i_{\rm M}$ of the current-controlled OS-CCM defined by Eq. (2b). Note that the expression $I_{\rm M}^2 = X + 2 \geq 0$ can be obtained by setting Eq. (2b) to zero, and the DC state variable X is bounded below by -2, i.e., $X \geq -2$. Figure 2(b) indicates the odd-symmetry of the current-controlled OS-CCM, which induces two symmetrical NDR regions, whose enlargements are illustrated in Figs. 2(a) and 2(c). Unlike the original current-controlled CCM defined by Eq. (1), which contains only a single NDR region in Fig. 1(b), the novel CCM sibling, dubbed the current-controlled OS-CCM, incorporates two symmetrical NDR regions with the current ranges -31.6 mA $< I_{\rm M} < -14.14$ mA and 14.14 mA $< I_{\rm M} <$ 31.6 mA. The symmetrical NDR regions, the fingerprint for symmetrical local activity, endow the memristor with the potential to generate symmetrical neuromorphic dynamics and symmetrical Turing instability.

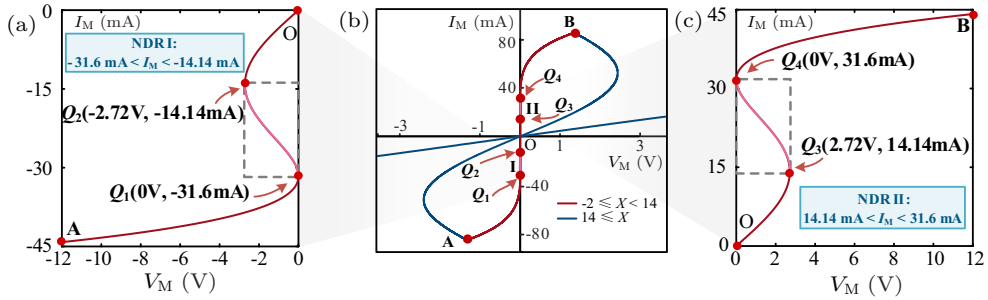


Fig. 2. DC $V_{\rm M}$–$I_{\rm M}$ characteristic of the current-controlled OS-CCM. (a) Enlarged view of the bottom red S-shaped branch I, showing the first NDR region within -2.72 V $< V_{\rm M} < 0$ V and -31.6 mA $< I_{\rm M} < -14.14$ mA, enclosed within a gray dashed box bounded by points Q_1 and Q_2. (b) Complete two-branch DC $V_{\rm M}$–$I_{\rm M}$ curve of the current-controlled OS-CCM, indicating its odd-symmetrical property. (c) Enlarged view of the above red S-shaped branch II, showing the second NDR region within 0 V $< V_{\rm M} <$ 2.72 V and 14.14 mA $< I_{\rm M} <$ 31.6 mA, enclosed within a gray dashed box bounded by points Q_3 and Q_4. The horizontal axes adopt different voltage units for the sake of clarity.

Note that to comprehensively capture the odd-symmetrical corsage-shaped DC $V_{\rm M}$–$I_{\rm M}$ curve of the current-controlled OS-CCM, the voltage $V_{\rm M}$ on the x-axis of Fig. 2(b) is expanded to [−3.5 kV, 3.5 kV]. The operating points in its two mirror-symmetrical NDR domains, where symmetrical Turing instability can be observed, are confined to -2.72 V $< V_{\rm M} < 0$ V, -31.6 mA $< I_{\rm M} < -14.14$ mA and 0 V $< V_{\rm M} <$ 2.72 V, 14.14 mA $< I_{\rm M} <$ 31.6 mA, which ensures feasible hardware implementation of the symmetrical Turing instability.

2.1. Symmetrical local activity and edge of chaos

The excitable and spiking-like responses, and other destabilization phenomena occur in memristive circuits when they operate at the edge of chaos in parameter regions, a subset of locally active domains that retain local asymptotic stability.[3] In order to verify whether the current-controlled OS-CCM can generate instability phenomena, we employed Chua's local activity and edge of chaos theory to accurately calculate its local-activity and edge of chaos domains.

For a current-controlled memristive circuit, the edge of chaos domain can be identified through the small-signal impedance function $Z(s, Q)$ at an equilibrium point Q; that is, the circuit is considered to operate at the edge of chaos if the following two criteria are simultaneously satisfied.

(I) **Local activity condition:** The real part of the impedance in the frequency domain becomes negative over a finite frequency interval, i.e., $\mathrm{Re}[Z(\mathrm{i}\omega, Q)] < 0$ for some ω.

(II) **Local asymptotic-stability condition:** All poles of the impedance function $Z(s, Q)$ are strictly located in the open left half-plane, i.e., $\mathrm{Re}[s_{\rm p}] < 0$.

The DC $V_{\rm M}$–$I_{\rm M}$ characteristic of the current-controlled OS-CCM in Fig. 2 indicates that the NDR regions, where instability phenomena can be observed, are confined to the branch corresponding to $-2 \leq X < 14$. Within this range, the relationships among the state variable X, the voltage $V_{\rm M}$, and the current $I_{\rm M}$ are given as follows:

$$V_{\rm M} = 75X^2 I_{\rm M}, \tag{3}$$

$$X = 2000 I_{\rm M}^2 - 2. \tag{4}$$

Based on the impedance formulation previously derived for the current-controlled CCM in our work,[5] the small-signal

impedance function $Z(s,Q)$ of the current-controlled OS-CCM at the equilibrium point Q can be expressed as follows:

$$Z(s,Q)=\frac{GX^2s+GKX^2+4GI_{\rm M}^2KTX}{s+K}. \tag{5}$$

From Eq. (5), the impedance $Z(s,Q)$ possesses the only negative pole $s_{\rm p}=-K=-10^4<0$, indicating that the current-controlled OS-CCM remains asymptotically-stable in the red branch with $-2\leq X<14$. The impedance function in the frequency domain by substituting $s=\mathrm{i}\omega$ into Eq. (5) is derived. The corresponding real part $\mathrm{Re}[Z(\mathrm{i}\omega,Q)]$ can be obtained as follows:

$$\mathrm{Re}[Z(\mathrm{i}\omega,Q)]=\frac{GX^2\omega^2+GK^2X^2+4GTI_{\rm M}^2K^2X}{\omega^2+K^2}. \tag{6}$$

To evaluate the local activity of the current-controlled OS-CCM, the three-dimensional distribution of $\mathrm{Re}[Z(\mathrm{i}\omega,Q)]$ as a function of ω and $I_{\rm M}$, and the corresponding parameter map are plotted in Fig. 3.

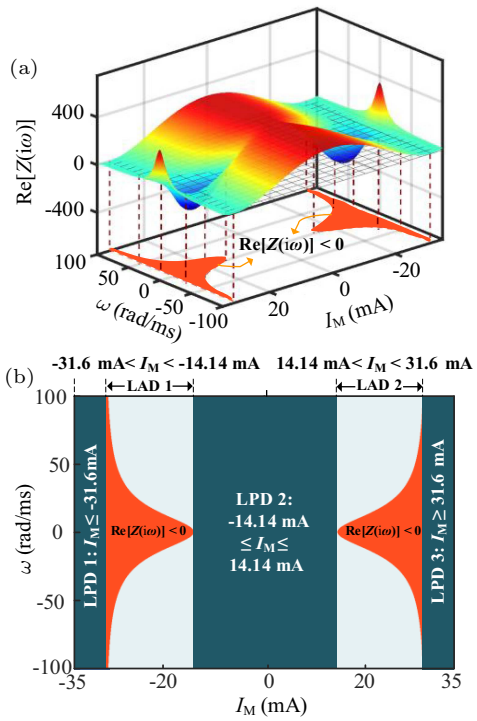


Fig. 3. (a) Three-dimensional distribution of $\mathrm{Re}[Z(\mathrm{i}\omega,Q)]$ of the current-controlled OS-CCM over -100 rad/ms $<\omega<100$ rad/ms and -35 mA $<I_{\rm M}<35$ mA ($-2\leq X<0.45$), with a projection of the contour $\mathrm{Re}[Z(\mathrm{i}\omega,Q)]=0$ superimposed at the bottom. (b) Color-coded parameter map of the current-controlled OS-CCM in the ω vs. $I_{\rm M}$ plane, where the red regions (locally active domains, LADs) represent $\mathrm{Re}[Z(\mathrm{i}\omega,Q)]<0$ and the remaining regions (locally passive domains, LPDs) denote $\mathrm{Re}[Z(\mathrm{i}\omega,Q)]>0$.

Figure 3(a) displays the landscape of $\mathrm{Re}[Z(\mathrm{i}\omega,Q)]$ defined by Eq. (6), superimposed with the red projection at the bottom, where the equilibrium points Q of the current-controlled OS-CCM satisfy $\mathrm{Re}[Z(\mathrm{i}\omega,Q)]<0$. The color-coded parameter map in the ω vs. $I_{\rm M}$ plane, i.e., the bottom plane shown in Fig. 3(a), is plotted in Fig. 3(b). From Fig. 3(b), the red regions denote $\mathrm{Re}[Z(\mathrm{i}\omega,Q)]<0$; that is, the current-controlled OS-CCM satisfies $\mathrm{Re}[Z(\mathrm{i}\omega,Q)]<0$ for some ω when it operates at two symmetrical current ranges, -31.6 mA $<I_{\rm M}<-14.14$ mA and 14.14 mA $<I_{\rm M}<$ 31.6 mA. Applying the local-activity condition, the current-controlled OS-CCM is locally active in this range. Also, since the negative pole $s_{\rm p}=-K=-10^4<0$ is derived by Eq. (5), the current-controlled OS-CCM satisfies the local asymptotic-stability condition; that is, it is stable for all the equilibrium points Q with $X<14$. The results indicate that the current-controlled OS-CCM is locally active and stable, i.e., at the edge of chaos, over the ranges -31.6 mA $<I_{\rm M}<-14.14$ mA and 14.14 mA $<I_{\rm M}<31.6$ mA. For the remaining cyan regions in Fig. 3(b), the current-controlled OS-CCM satisfies $\mathrm{Re}[Z(\mathrm{i}\omega,Q)]>0$ for all ω, indicating it is locally passive in this parameter range, where sustained oscillation and spiking responses cannot be supported. Owing to the symmetry of the memristor, the resulting parameter maps exhibit symmetry with respect to the zero-bias axis. The symmetrical edge-of-chaos domains indicate that the memristor proposed in this work possesses the capability to generate symmetrical Turing instability.

2.2. Single cell made of a current-controlled OS-CCM

When the current-controlled OS-CCM operates at the equilibrium point within the range -31.6 mA $<I_{\rm M}<-14.14$ mA and 14.14 mA $<I_{\rm M}<31.6$ mA, it is on the edge of chaos, as demonstrated in Fig. 3, where it exhibits the capability to form a neuron cell. To better emulate the external excitation of biological cells using voltage signals, the memristor cell was redesigned from a current-driven to a voltage-driven configuration via Kirchhoff's circuit laws, as illustrated in Fig. 4.

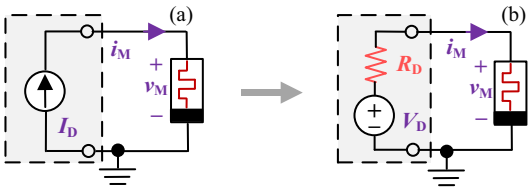


Fig. 4. (a) Current-biased cell made of a current-controlled OS-CCM, where a DC current source $I_{\rm D}$ drives the memristor. (b) Equivalent voltage-biased cell obtained by replacing the current source $I_{\rm D}$ with an ideal voltage source $V_{\rm D}$ in series with a resistor $R_{\rm D}$.

As illustrated in Fig. 4(a), the current-controlled OS-CCM is directly driven by an ideal DC current source $I_{\rm D}$, which provides the memristor current $i_{\rm M}$ and the corresponding terminal voltage $v_{\rm M}$. Figure 4(b) shows an equivalent voltage-driven realization, where the current excitation is replaced by an ideal voltage source $V_{\rm D}$ in series with a resistor $R_{\rm D}$, where the voltage source $V_{\rm D}$ provides a more direct analogy to external excitation in biological cells. This transformation follows directly from Kirchhoff's current law, ensuring

that the resulting current $i_{\rm M}$ and terminal voltage $v_{\rm M}$ are identical to those obtained in the current-driven configuration. Consequently, the operating point Q of the current-controlled OS-CCM is preserved, and the voltage-driven realization shown in Fig. 4(b) can be used without altering the local activity of the memristor.

To guarantee that the voltage-biased cell in Fig. 4(b) operates within the desired edge-of-chaos domains, the series resistor $R_{\rm D}$ must satisfy the following condition (note that as $X < 14$, the expression $X = TI_{\rm M}^2 - 2$ can be derived by setting Eq. (2b) to zero):

$$R_{\rm D} > \left|\frac{{\rm d}V_{\rm M}}{{\rm d}I_{\rm M}}\right| = \left|\frac{{\rm d}(R(X)I_{\rm M})}{{\rm d}I_{\rm M}}\right| = \left|5GT^2I_{\rm M}^4 - 12GTI_{\rm M}^2 + 4G\right|. \tag{7}$$

For the bias point $P_2(V_{\rm M}, I_{\rm M}) = (2.16\ {\rm V}, 20\ {\rm mA})$ with $X = -1.2$, which lies near the center of the locally active domain II (NDR II) of the current-controlled OS-CCM, as shown in Fig. 5(b), the minimum permissible value of the series resistor $R_{\rm D}$ is 180 Ω, i.e., $R_{\rm D} > 180\ \Omega$. If $R_{\rm D} \leq 180\ \Omega$, the slope of the load line becomes too steep, causing the load line to intersect the DC $V_{\rm M}$–$I_{\rm M}$ curve at an unstable operating point, and the current-controlled OS-CCM will lose the conditions required for generating Turing instability. Hence, $R_{\rm D} = 330\ \Omega$ is selected in the cell to construct the Turing circuit.

To illustrate the load-line constraint imposed by the series resistor $R_{\rm D}$ and its impact on the admissible operating points, the intersections between the load line and the enlarged DC $V_{\rm M}$–$I_{\rm M}$ characteristic of the current-controlled OS-CCM are shown in Fig. 5.

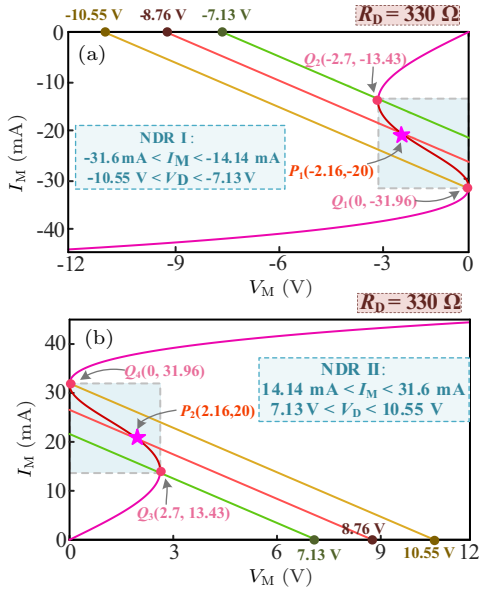


Fig. 5. Load-line intersections of the current-controlled OS-CCM with the enlargement NDR domain I, bounded by Q_2 (−2.7 V, −13.43 mA) and Q_1 (0 V, −31.96 mA) in (a) and with the enlargement NDR domain II, bounded by Q_3 (2.7 V, 13.43 mA) and Q_4 (0 V, 31.96 mA) in (b). All slanted lines in the figure are load lines corresponding to the adopted series resistance $R_{\rm D} = 330\ \Omega$.

Figure 5(a) shows that the cell in Fig. 4(b) operates in the NDR domain I only when the bias voltage $V_{\rm D}$ is confined to a finite interval between −10.55 V and −7.13 V, i.e., when $-10.55\ {\rm V} < V_{\rm D} < -7.13\ {\rm V}$. Similarly, when the bias voltage $V_{\rm D}$ of the cell satisfies $7.13\ {\rm V} < V_{\rm D} < 10.55\ {\rm V}$, it maintains its local activity, as demonstrated in Fig. 5(b). When $V_{\rm D}$ lies outside this interval, the load line intersects only positive-slope branches, forcing the operating point into a locally passive domain where Turing instability cannot be observed.

The bias voltage ranges corresponding to the negative NDR domain I and the positive NDR domain II are symmetrically distributed with respect to the origin, reflecting the intrinsic odd symmetry of the current-controlled OS-CCM. From Fig. 5, when the bias voltages of the cell are $V_{\rm D} = -8.76$ V and $V_{\rm D} = 8.76$ V, the red load lines within the respective admissible voltage ranges intersect the DC $V_{\rm M}$–$I_{\rm M}$ curve in the NDR I and NDR II regions, respectively. This ensures that the operating points remain robustly confined within the locally active domains and provides a consistent operating-point basis for the realization of symmetrical Turing instability.

In this section, a novel CCM sibling, dubbed the current-controlled OS-CCM, was constructed, and a cell constructed using only the CCM sibling was presented, whose odd-symmetrical locally active and edge of chaos domain provides a necessary condition for the emergence of symmetrical Turing instability.

3. Two-cell network exhibiting symmetrical Turing instability

This section presents a two-cell network to observe symmetrical Turing instability. Each cell is constructed solely from a current-controlled OS-CCM and is coupled together with a passive resistor $R_{\rm C}$ that serves as the control parameter. The intrinsic odd symmetry of the current-controlled OS-CCM, as demonstrated in the previous section, leads to mirrored dynamics under positive and negative bias, enabling the emergence of symmetrical Turing instability. The network structure is shown in Fig. 6.

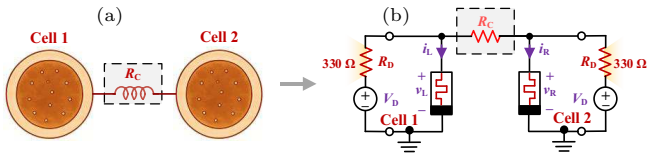


Fig. 6. Symmetrical OS-CCMs-based two-cell network. (a) Conceptual diagram of two biological cells coupled via a synapse with a strength of $R_{\rm C}$. (b) Circuit realization of two-cell network, where each cell is constructed with a current-controlled OS-CCM, biased by a DC source $V_{\rm D}$ of ±8.76 V in series with a resistor $R_{\rm D}$ of 330 Ω.

The two-cell network, as shown in Fig. 6(b), consists of two identical current-controlled OS-CCM-based cells, resembling the biological cellular structure depicted in Fig. 6(a). In Fig. 6(b), each cell is biased by the same DC source $V_{\rm D} =$

± 8.76 V through an identical series resistor $R_{\mathrm{D}} = 330\ \Omega$, and the two cells are coupled by a passive resistor R_{C}. As $V_{\mathrm{D}} = \pm 8.76$ V and $R_{\mathrm{D}} = 330\ \Omega$, the two cells are locally active and stable, as demonstrated in Fig. 5. By varying R_{C}, the coupling strength can be continuously tuned, further inducing the emergence of instability in the network.

To analyze the effect of the coupling resistor R_{C} on the stability of the equilibrium points Q of the network, one can derive the state equations of the two-cell network in Fig. 6(b) as follows:

$$\frac{\mathrm{d}x_{\mathrm{L}}}{\mathrm{d}t} = 10^4(30 - x_{\mathrm{L}} + |x_{\mathrm{L}} - 14| - |x_{\mathrm{L}} - 46| + 2000i_{\mathrm{L}}^2), \quad (8a)$$

$$\frac{\mathrm{d}x_{\mathrm{R}}}{\mathrm{d}t} = 10^4(30 - x_{\mathrm{R}} + |x_{\mathrm{R}} - 14| - |x_{\mathrm{R}} - 46| + 2000i_{\mathrm{R}}^2), \quad (8b)$$

where x_{L} and x_{R} denote the state variables of the two-cell network, which are the internal states of the left and right current-controlled OS-CCMs, respectively. Likewise, i_{L} and v_{L} (resp. i_{R} and v_{R}) represent the left (resp. right) memristor current and voltage. Applying Kirchhoff's law and Ohm's law, one can obtain the following expressions:

$$i_{\mathrm{L}} = \frac{V_{\mathrm{D}} - R_{\mathrm{L}} i_{\mathrm{L}}}{R_{\mathrm{D}}} - \frac{R_{\mathrm{L}} i_{\mathrm{L}} - R_{\mathrm{R}} i_{\mathrm{R}}}{R_{\mathrm{C}}}, \quad (9a)$$

$$i_{\mathrm{R}} = \frac{V_{\mathrm{D}} - R_{\mathrm{R}} i_{\mathrm{R}}}{R_{\mathrm{D}}} + \frac{R_{\mathrm{L}} i_{\mathrm{L}} - R_{\mathrm{R}} i_{\mathrm{R}}}{R_{\mathrm{C}}}, \quad (9b)$$

where $R_{\mathrm{L}} = G x_{\mathrm{L}}^2$ and $R_{\mathrm{R}} = G x_{\mathrm{R}}^2$ denote the memristance of the left and right current-controlled OS-CCMs, respectively. Solving Eqs. (9) provides

$$i_{\mathrm{L}} = \frac{V_{\mathrm{D}}(2R_{\mathrm{D}}R_{\mathrm{R}} + R_{\mathrm{D}}R_{\mathrm{C}} + R_{\mathrm{R}}R_{\mathrm{C}})}{R_{\mathrm{D}}^2R_{\mathrm{L}} + R_{\mathrm{D}}^2R_{\mathrm{R}} + R_{\mathrm{D}}^2R_{\mathrm{C}} + 2R_{\mathrm{D}}R_{\mathrm{L}}R_{\mathrm{R}} + R_{\mathrm{D}}R_{\mathrm{L}}R_{\mathrm{C}} + R_{\mathrm{D}}R_{\mathrm{R}}R_{\mathrm{C}} + R_{\mathrm{L}}R_{\mathrm{R}}R_{\mathrm{C}}}, \quad (10a)$$

$$i_{\mathrm{R}} = \frac{V_{\mathrm{D}}(2R_{\mathrm{D}}R_{\mathrm{L}} + R_{\mathrm{D}}R_{\mathrm{C}} + R_{\mathrm{L}}R_{\mathrm{C}})}{R_{\mathrm{D}}^2R_{\mathrm{L}} + R_{\mathrm{D}}^2R_{\mathrm{R}} + R_{\mathrm{D}}^2R_{\mathrm{C}} + 2R_{\mathrm{D}}R_{\mathrm{L}}R_{\mathrm{R}} + R_{\mathrm{D}}R_{\mathrm{L}}R_{\mathrm{C}} + R_{\mathrm{D}}R_{\mathrm{R}}R_{\mathrm{C}} + R_{\mathrm{L}}R_{\mathrm{R}}R_{\mathrm{C}}}. \quad (10b)$$

3.1. Critical value of the symmetrical Turing instability

To accurately calculate the critical value of the coupling resistance for the emergence of symmetric Turing instability, the eigenvalues of the Jacobian matrix associated with the state equations at the equilibrium point Q need to be obtained. The 2×2 Jacobian matrix J, which linearizes the state equations in Eq. (8) around the equilibrium point Q, is obtained by substituting the steady-state operating-point parameters into the implicit differentiation, yielding the explicit Jacobian matrix as follows:

$$J = \begin{bmatrix} J_{11} & J_{12} \\ J_{21} & J_{22} \end{bmatrix} = \begin{bmatrix} \left.\frac{\partial f_1}{\partial x_{\mathrm{L}}}\right|_Q & \left.\frac{\partial f_1}{\partial x_{\mathrm{R}}}\right|_Q \\ \left.\frac{\partial f_2}{\partial x_{\mathrm{L}}}\right|_Q & \left.\frac{\partial f_2}{\partial x_{\mathrm{R}}}\right|_Q \end{bmatrix}, \quad (11)$$

where the elements are

$$\begin{aligned}
J_{11} &= -K((2TV_{\mathrm{D}}^2(R_{\mathrm{C}}R_{\mathrm{D}} + GR_{\mathrm{C}}X_{\mathrm{R}}^2 + 2GR_{\mathrm{D}}X_{\mathrm{R}}^2)^2(4X_{\mathrm{L}}G^2R_{\mathrm{D}}X_{\mathrm{R}}^2 + 2R_{\mathrm{C}}X_{\mathrm{L}}G^2X_{\mathrm{R}}^2 + 2X_{\mathrm{L}}GR_{\mathrm{D}}^2 + 2R_{\mathrm{C}}X_{\mathrm{L}}GR_{\mathrm{D}}))/D^3 + 1), \\
J_{12} &= K((2TV_{\mathrm{D}}^2(2GR_{\mathrm{C}}X_{\mathrm{R}} + 4GR_{\mathrm{D}}X_{\mathrm{R}})(R_{\mathrm{C}}R_{\mathrm{D}} + GR_{\mathrm{C}}X_{\mathrm{R}}^2 + 2GR_{\mathrm{D}}X_{\mathrm{R}}^2))/(2G^2R_{\mathrm{D}}X_{\mathrm{L}}^2X_{\mathrm{R}}^2 + R_{\mathrm{C}}G^2X_{\mathrm{L}}^2X_{\mathrm{R}}^2 + GR_{\mathrm{D}}^2X_{\mathrm{L}}^2 \\
&\quad + GR_{\mathrm{D}}^2X_{\mathrm{R}}^2 + R_{\mathrm{C}}GR_{\mathrm{D}}X_{\mathrm{L}}^2 + R_{\mathrm{C}}GR_{\mathrm{D}}X_{\mathrm{R}}^2 + R_{\mathrm{C}}R_{\mathrm{D}}^2)^2 \\
&\quad - (2TV_{\mathrm{D}}^2(R_{\mathrm{C}}R_{\mathrm{D}} + GR_{\mathrm{C}}X_{\mathrm{R}}^2 + 2GR_{\mathrm{D}}X_{\mathrm{R}}^2)^2(4X_{\mathrm{R}}G^2R_{\mathrm{D}}X_{\mathrm{L}}^2 + 2R_{\mathrm{C}}X_{\mathrm{R}}G^2X_{\mathrm{L}}^2 + 2X_{\mathrm{R}}GR_{\mathrm{D}}^2 + 2R_{\mathrm{C}}X_{\mathrm{R}}GR_{\mathrm{D}}))/D^3), \\
J_{21} &= K((2TV_{\mathrm{D}}^2(2GR_{\mathrm{C}}X_{\mathrm{L}} + 4GR_{\mathrm{D}}X_{\mathrm{L}})((R_{\mathrm{C}}R_{\mathrm{D}} + GR_{\mathrm{C}}X_{\mathrm{L}}^2 + 2GR_{\mathrm{D}}X_{\mathrm{L}}^2))/(2G^2R_{\mathrm{D}}X_{\mathrm{L}}^2X_{\mathrm{R}}^2 + R_{\mathrm{C}}G^2X_{\mathrm{L}}^2X_{\mathrm{R}}^2 \\
&\quad + GR_{\mathrm{D}}^2X_{\mathrm{L}}^2 + GR_{\mathrm{D}}^2X_{\mathrm{R}}^2 + R_{\mathrm{C}}GR_{\mathrm{D}}X_{\mathrm{L}}^2 + R_{\mathrm{C}}GR_{\mathrm{D}}X_{\mathrm{R}}^2 + R_{\mathrm{C}}R_{\mathrm{D}}^2)^2 \\
&\quad - (2TV_{\mathrm{D}}^2(R_{\mathrm{C}}R_{\mathrm{D}} + GR_{\mathrm{C}}X_{\mathrm{L}}^2 + 2GR_{\mathrm{D}}X_{\mathrm{L}}^2)^2(4X_{\mathrm{L}}G^2R_{\mathrm{D}}X_{\mathrm{R}}^2 + 2R_{\mathrm{C}}X_{\mathrm{L}}G^2X_{\mathrm{R}}^2 + 2X_{\mathrm{L}}GR_{\mathrm{D}}^2 + 2R_{\mathrm{C}}X_{\mathrm{L}}GR_{\mathrm{D}}))/D^3), \\
J_{22} &= -K((2TV_{\mathrm{D}}^2(R_{\mathrm{C}}R_{\mathrm{D}} + GR_{\mathrm{C}}X_{\mathrm{L}}^2 + 2GR_{\mathrm{D}}X_{\mathrm{L}}^2)^2(4X_{\mathrm{R}}G^2R_{\mathrm{D}}X_{\mathrm{L}}^2 + 2R_{\mathrm{C}}X_{\mathrm{R}}G^2X_{\mathrm{L}}^2 + 2X_{\mathrm{R}}GR_{\mathrm{D}}^2 + 2R_{\mathrm{C}}X_{\mathrm{R}}GR_{\mathrm{D}}))/D^3 + 1) \\
D &= 2G^2R_{\mathrm{D}}X_{\mathrm{L}}^2X_{\mathrm{R}}^2 + R_{\mathrm{C}}G^2X_{\mathrm{L}}^2X_{\mathrm{R}}^2 + R_{\mathrm{C}}GR_{\mathrm{D}}X_{\mathrm{L}}^2 + GR_{\mathrm{D}}^2X_{\mathrm{L}}^2 + GR_{\mathrm{D}}^2X_{\mathrm{R}}^2 + R_{\mathrm{C}}GR_{\mathrm{D}}X_{\mathrm{R}}^2 + R_{\mathrm{C}}R_{\mathrm{D}}^2,
\end{aligned}$$

and $K = 10^4$, $G = 75$, $V_{\mathrm{D}} = \pm 8.76$ V, $R_{\mathrm{D}} = 330\ \Omega$, $T = 2000$.

The characteristic equation to calculate the eigenvalues, derived from the Jacobian matrix J in Eq. (12), is as follows:

$$\lambda^2 - (J_{11} + J_{22})\lambda + J_{11}J_{22} - J_{12}J_{21} = 0. \quad (12)$$

The stability of the operating point Q is determined by solving the characteristic equation of the Jacobian matrix J, defined by Eq. (12), and examining the resulting eigenvalues, λ_1 and λ_2. If the real parts of both eigenvalues $\lambda_{1,2}$ satisfy $\mathrm{Re}[\lambda] < 0$, the operating point Q is asymptotically stable and no instability phenomena occur. Conversely, if any one of its eigenvalues satisfies $\mathrm{Re}[\lambda] > 0$, the equilibrium becomes unstable, indicating the onset of Turing instability.

To determine the critical coupling condition for triggering Turing instability, the eigenvalue trajectories of the two-cell Jacobian are plotted as the coupling resistor R_C is swept in Fig. 7.

As shown in Fig. 7, the stability of the two-cell network in Fig. 6(b) is governed by the evolution of its two eigenvalues $\lambda_{1,2}$ as the coupling resistor R_C is reduced. Over a wide range of weak coupling with the coupling resistance $R_C > 792\ \Omega$, both eigenvalues $\lambda_{1,2}$ stay negative and the symmetrical equilibrium remains stable. In particular, the varying eigenvalue λ_2 is negative at $R_C = 8\ \text{k}\Omega$ with $\lambda_2 = -3024$, at $R_C = 5\ \text{k}\Omega$ with $\lambda_2 = -2791$, and at $R_C = 1.5\ \text{k}\Omega$ with $\lambda_2 = -1457$. Also, λ_1 stays negative and is constant around $\lambda_1 = -3424$ throughout the entire sweep. When R_C is decreased to 792 Ω, λ_2 reaches zero and crosses into the positive half-plane. For stronger coupling below this threshold, λ_2 becomes positive, for example, $\lambda_2 = 1509$ at $R_C = 500\ \Omega$, indicating the loss of stability for the two-cell network. Therefore, the coupling resistance at $R_{C0} = 792\ \Omega$ is identified as the critical value for triggering Turing instability in the proposed two-cell network, that is, the network is stable for $R_C > 792\ \Omega$, and becomes unstable once R_C is reduced below the critical value of 792 Ω.

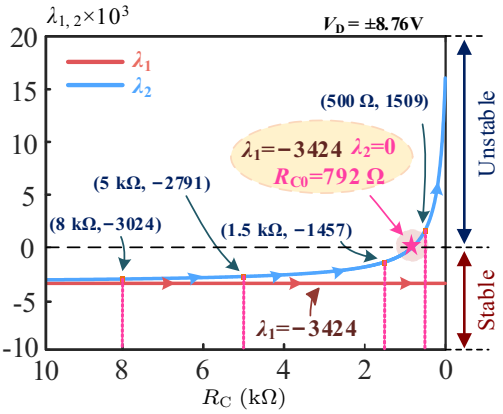


Fig. 7. Eigenvalue trajectories of the two-cell network as the coupling resistor R_C is varied, showing the zero-crossing point of the pole λ_2 (blue curve) at $R_C = 792\ \Omega$. Also shown is the constant negative value of the pole λ_1 (red curve).

3.2. Symmetrical Turing instability

To reveal how the coupling resistor R_C controls the transition from symmetrical steady operation to coupling-induced symmetry-breaking, the time-domain responses of the two state variables x_R and x_L under representative coupling strengths are displayed in Fig. 8.

Figure 8 compares the time-domain evolutions of the two state variables x_L and x_R under different coupling resistances at the positive and negative input voltages $V_D = \pm8.76$ V, providing a direct dynamical view of how the steady state reorganizes as R_C is reduced. In Fig. 8(a) for $R_C = 5\ \text{k}\Omega$, the two trajectories rapidly converge to the same asymptotically stable state with $X_L = X_R = -1.2$, indicating that the stability of the two cells remains unbroken. In Figs. 8(b) and Fig. 8(c), when R_C is reduced to 680 Ω and 580 Ω, the two state variables no longer converge to the original stable state variables, while X_L settles near −1.58 and −1.63, and X_R approaches −0.17 and −0.05, respectively. Figures 8(b) and 8(c) reveal a clear separation of the final operating states between the two cells, indicating the emergence of an instability phenomenon, aka, Turing instability. In Fig. 8(d) with $R_C = 18\ \Omega$, this separation becomes more pronounced with a gap of 2.65. These results show that decreasing R_C strengthens the dissipative coupling and drives the network from identical steady-state convergence to a split steady-state outcome, that is, the two cells settle at distinct operating states.

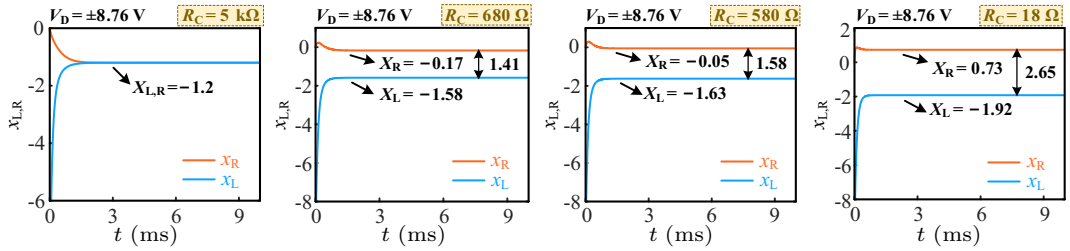


Fig. 8. Time-domain responses of state variables x_R and x_L of the two-cell network at $V_D = \pm8.76$ V for different coupling resistances R_C. (a) Two state variables x_R and x_L converge to the same stable state variables at $X_L = X_R = -1.2$ with $R_C = 5\ \text{k}\Omega$. (b) The stable state variables of x_R and x_L split into $X_L = -1.58$ and $X_R = -0.17$ with $R_C = 680\ \Omega$, showing symmetry-breaking phenomenon. The gap of the stable state variables of x_R and x_L increases to 1.58 with $R_C = 580\ \Omega$ in (c) and to 2.65 with $R_C = 18\ \Omega$ in (d), showing wider separation for strong coupling.

To further clarify how the final steady state evolves as R_C varies, Fig. 9 summarizes the R_C-dependent steady-state branches obtained by continuously sweeping R_C from 0 to 2.5 kΩ, with representative time-domain cases shown for comparison.

Figure 9(b) illustrates the evolution of the stable states of two state variables for the network with respect to the coupling resistance R_C. When $R_C > 792\ \Omega$, the state variable X_L of the steady state for the left cell coincides with that for the right cell, i.e., $X_L = X_R$. As $R_C < 792\ \Omega$, the two steady-state variables separate into two distinct branches, and the gap between X_L and X_R becomes larger as R_C is further decreased. These results indicate that R_C determines both the critical coupling condition for branch splitting and the resulting degree of steady-state separation between the two cells. Figure 9(a) gives a representative weak-coupling case with $R_C = 2\ \text{k}\Omega$,

where the two state variables relax to the same steady value at $X_L = X_R = -1.2$. Figure 9(c) shows a representative stronger-coupling case with $R_C = 400\ \Omega$, where the two state variables converge to distinct steady values $X_L = -1.71$ and $X_R = 0.16$, demonstrating a clear steady-state separation between the left and right cells in the network.

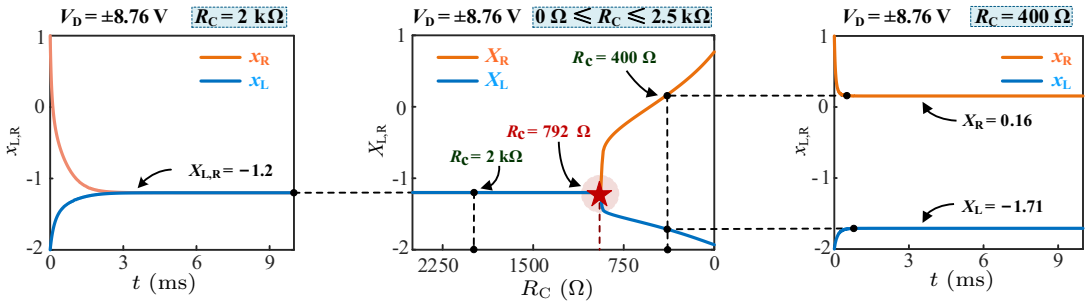


Fig. 9. R_C-dependent steady-state evolution of the two-cell network under $V_D = \pm 8.76$ V. (a) Representative time-domain case at $R_C = 2$ kΩ, where the two stable state variables converge to the same steady value $X_L = X_R = -1.2$. (b) Steady-state branches X_L and X_R obtained by sweeping R_C from 0 to 2.5 kΩ, showing a critical coupling value $R_{C0} = 792\ \Omega$ at which the single uniform branch splits into two distinct branches. (c) Representative time-domain case at $R_C = 400\ \Omega$, where the steady state variables separate to $X_L = -1.71$ and $X_R = 0.16$.

To visualize how the global flow in the (x_L, x_R) phase plane changes with coupling strength, Fig. 10 plots the basin of attraction, superimposed on the trajectories starting from different initial conditions for several representative values of R_C.

Figure 10 shows how the phase-plane flow in the (x_L, x_R) space changes as the coupling resistance R_C is reduced. For $R_C = 2$ kΩ in Fig. 10(a) and $R_C = 1$ kΩ in Fig. 10(b), trajectories launched from different initial conditions converge to the same stable equilibrium point at $O_1(X_L, X_R) = O_2(X_L, X_R) = (-1.2, -1.2)$, indicating that the two cells in the network approach an identical steady state under weak coupling with $R_C > 792\ \Omega$. For $R_C = 400\ \Omega$, the trajectories starting from different initial conditions separate into two basins; that is, the trajectories starting from initial conditions in the light blue region will converge to the point $O_3(X_L, X_R) = (-1.71, 0.16)$, while those beginning in the light orange region will converge to the point $O_4(X_L, X_R) = (0.16, -1.71)$, as shown in Fig. 10(c). From Fig. 10(d), the symmetry-breaking phenomenon persists and the separation between the two stable states $O_5(X_L, X_R) = (-1.87, 0.58)$ and $O_6(X_L, X_R) = (0.58, -1.87)$ becomes larger, indicating a stronger steady-state separation between x_L and x_R at $R_C = 100\ \Omega$. Figure 10 shows the transition from a single-equilibrium-point uniform state to a two-equilibrium-point non-uniform state as R_C decreases, providing a signature of coupling-induced symmetry-breaking associated with Turing instability.

To observe the symmetry property of the Turing instability, Fig. 11 plots the time-domain voltages v_L and v_R for different coupling resistances R_C, along with the evolution of v_L and v_R during a continuous sweep of R_C, showing the transition from a single shared steady state under weak coupling to two mirrored steady states after symmetry-breaking at stronger coupling.

Figure 11 provides a time-domain view of how the two voltages v_L and v_R of the left and right cells in the network evolve as the coupling resistor R_C is reduced under a fixed bias of $V_D = \pm 8.76$ V. For each subplot in Fig. 11, the upper waveform, above the black dashed line, is the trajectories of v_L and v_R under the positive bias voltage $V_D = 8.76$ V of the network, while the lower one corresponds to the trajectories under the opposite bias voltage $V_D = -8.76$ V. For the weak-coupling case with $R_C > 792\ \Omega$, both trajectories in Fig. 11(a) stabilize at the same stable states $V_L = V_R = 2.16$ V under the positive bias voltage $V_D = 8.76$ V, and the opposite states $V_L = V_R = -2.16$ V under $V_D = -8.76$ V. As the coupling resistance R_C is decreased into the range $R_C < 792\ \Omega$, a clear symmetry-breaking phenomenon appears under the positive and negative voltages, as shown in Figs. 11(b)–11(d).

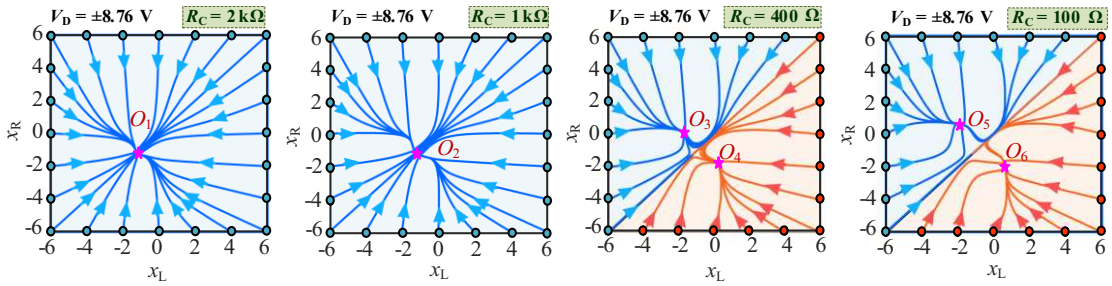


Fig. 10. Phase-plane trajectories in the (x_L, x_R) plane for $V_D = \pm 8.76$ V under different coupling resistances. (a) Trajectories of x_L and x_R starting from different initial conditions, all converging to the unique stable equilibrium point $O_1(X_L, X_R) = (-1.2, -1.2)$ at $R_C = 2$ kΩ. (b) Trajectories still converging to the unique stable equilibrium point $O_2(X_L, X_R) = (-1.2, -1.2)$ at $R_C = 1$ kΩ. (c) Emergence of steady-state separation at $R_C = 400\ \Omega$, where trajectories converge to two distinct stable equilibrium points $O_3(X_L, X_R) = (-1.71, 0.16)$ and $O_4(X_L, X_R) = (0.16, -1.71)$. (d) Further enhanced steady-state separation at $R_C = 100\ \Omega$, with trajectories converging to two distinct stable equilibrium points $O_5(X_L, X_R) = (-1.87, 0.58)$ and $O_6(X_L, X_R) = (0.58, -1.87)$.

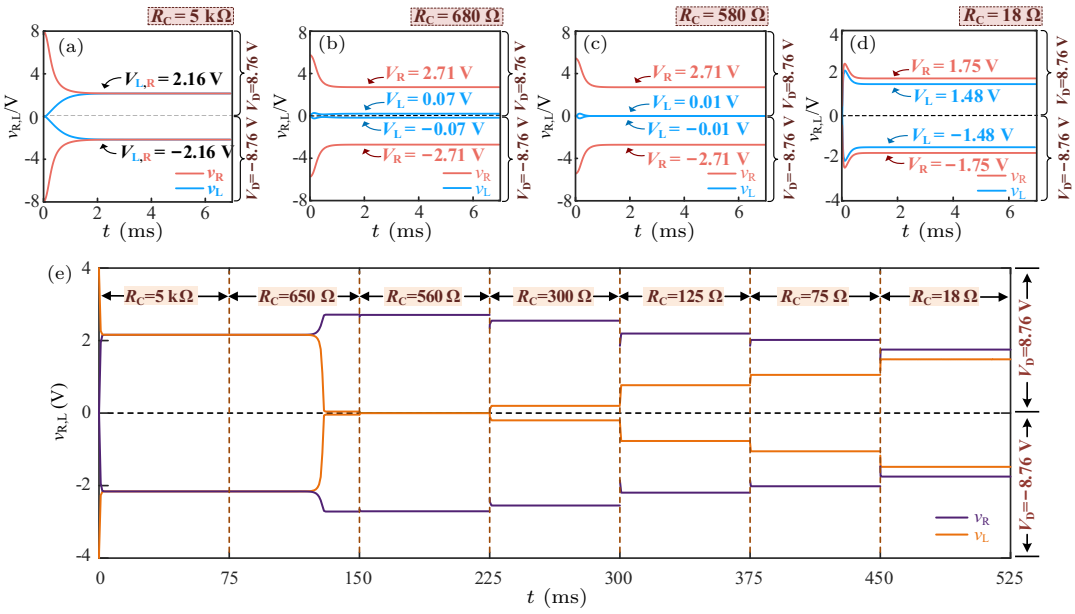


Fig. 11. Time-domain voltages v_L and v_R under $V_D = \pm 8.76$ V for different coupling resistances R_C: (a) $R_C = 5$ kΩ, $V_L = V_R = 2.16$ V at $V_D = 8.76$ V and $V_L = V_R = -2.16$ V at $V_D = -8.76$ V. (b) $R_C = 680$ Ω, $V_R = 2.71$ V and $V_L = 0.07$ V at $V_D = 8.76$ V, and $V_R = -2.71$ V and $V_L = -0.07$ V at $V_D = -8.76$ V; (c) $R_C = 580$ Ω, $V_R = 2.71$ V and $V_L = 0.01$ V at $V_D = 8.76$ V, and $V_R = -2.71$ V and $V_L = -0.01$ V at $V_D = -8.76$V; (d) $R_C = 18$ Ω, $V_R = 1.75$ V and $V_L = 1.48$ V at $V_D = 8.76$ V, and $V_R = -1.75$ V and $V_L = -1.48$ V at $V_D = -8.76$ V. (e) Symmetrical evolution of voltages v_L and v_R from a single stable state to distinct stable states.

From Fig. 11(b), the voltages v_L and v_R no longer converge to the same stable state; instead, they diverge into distinct stable states, namely, $V_R = 2.71$ V and $V_L = 0.07$ V under the positive bias voltage $V_D = 8.76$ V at $R_C = 680$ Ω, demonstrating the emergence of a symmetry-breaking phenomenon, aka, Turing instability. Similarly, an analogous symmetry-breaking destabilization is observed under the negative bias voltage $V_D = -8.76$ V, as evidenced by the lower trace in Fig. 11(b), where the voltages settle at $V_R = -2.71$ V and $V_L = -0.07$ V for the same $R_C = 680$ Ω under this negative bias condition. These four independent, asymptotically stable steady-state voltage operating points collectively constitute the quadristability of the coupled system, which represents a core dynamical hallmark of the symmetric Turing instability investigated herein.

Simulation results confirm the emergence of symmetrical Turing instability. For lower coupling resistance R_C, i.e., stronger coupling conditions, such as $R_C = 580$ Ω and $R_C = 18$ Ω, symmetrical Turing instability can still be observed, as shown in Figs. 11(c) and 11(d). Compared with the voltage separation gap in Figs. 11(b) and 11(c), the strong-coupling case in Fig. 11(d) does not further enlarge the voltage separation; instead, the gap $|V_L - V_R|$ decreases. This confirms that the voltage separation does not vary monotonically with R_C and may deviate from the splitting behavior observed in the internal state variables.

Figure 11(e) further illustrates the transition of the cell voltages v_L and v_R from identical stable states to distinct stable states, demonstrating the emergence of symmetrical Turing instability. The coupling resistance R_C can also adjust the separation distance between the stable states of the cell voltages. In particular, Fig. 11(e) clearly captures the emergence of a strongly asymmetric plateau pair in the intermediate-R_C stages (around 650 Ω–560 Ω), where one state remains near a high-magnitude level while the other stays close to zero, consistent with the steady-state values highlighted in Figs. 11(b) and 11(c). Toward the end of the sweep, at smaller R_C values, the plateau levels redistribute and partially rebalance, consistent with the reduced separation observed in Fig. 11(d).

To investigate the relationship between the voltage separation distance and the coupling resistance R_C, we next continuously sweep R_C under $V_D = \pm 8.76$ V and summarize the resulting steady-voltage trajectories in Fig. 12.

Figure 12 summarizes the steady-state voltages as R_C is swept under $V_D = \pm 8.76$ V, further demonstrating the emergence of the symmetrical destabilization phenomenon. For $R_C > R_{C0} = 792$ Ω, the two cells settle at the same voltage level, so the steady-state voltage difference between V_R and V_L is zero. When R_C is reduced below 792 Ω, the steady-state voltages split into two branches and V_R and V_L become different. As $R_C < 792$ Ω, the voltage separation distance first increases until reaching its maximum of 2.71 V at $R_C = 560$ Ω, and then gradually decreases. As the coupling resistance R_C tends to zero, they nearly converge back together.

In this section, a two-cell OS-CCM network was formulated for the demonstration of symmetrical Turing instability, and the critical coupling resistance for observing the destabilization phenomenon was quantitatively determined. The stability of the cells was demonstrated to be disrupted by the coupling resistance under both positive and negative bias voltages, giving rise to the observation of symmetrical Turing instability.

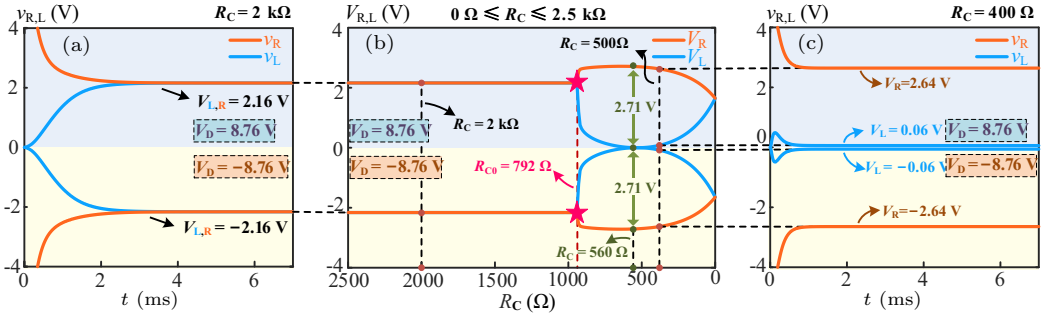


Fig. 12. Voltage-level steady-state behavior of the two-cell network under symmetrical excitation $V_D = \pm 8.76$ V as the coupling resistor R_C is varied. (a) Representative time-domain response at $R_C = 2$ kΩ, where the two cell voltages coincide at $V_R = V_L = 2.16$ V for $V_D = 8.76$ V and $V_R = V_L = -2.16$ V for $V_D = -8.76$ V. (b) Steady-state trajectories of V_R and V_L obtained by scanning R_C over $0\ \Omega \le R_C \le 2.5$ kΩ, marking the critical coupling value $R_{C0} = 792\ \Omega$. (c) Representative time-domain response at $R_C = 400\ \Omega$, where the voltages separate to $V_R = 2.64$ V and $V_L = 0.06$ V for $V_D = 8.76$ V, and $V_R = -2.64$ V and $V_L = -0.06$ V for $V_D = -8.76$ V.

4. Hardware demonstration of symmetrical Turing instability

This section presents the hardware validation of symmetrical Turing instability using two homemade current-controlled OS-CCM circuit boards. The hardware realization of the cell is based on an OS-CCM circuit board, and the experimentally measured symmetrical Turing instability is introduced here.

4.1. Hardware implementation of OS-CCM

A homemade current-controlled CCM circuit board has been reported in our work.[5] Here, the hardware implementation of the current-controlled OS-CCM is introduced; its schematic diagram is shown in Fig. 13. It provides the experimental setup for the two-cell coupling experiments reported in the following subsections.

The current-controlled OS-CCM is implemented as a one-port memristive element, described by the equations $v_M = R(x, i_M) i_M$ with an internal state variable governed by $\mathrm{d}x/\mathrm{d}t = f(x, i_M)$. As shown in Fig. 13(a), the memristor is interfaced only through its terminal voltage v_M and current i_M. Figure 13(b) presents the analog circuit that realizes the equations describing the relationship between voltage v_M and current i_M. The derivation of the circuit in Fig. 13(b) follows the same procedure as reported in our work,[19] and is omitted here. The OS-CCM physical circuit contains five op-amps, three analog multipliers, one capacitor, and 33 resistors, where U_1–U_5 are a two-channel TL082CN op-amp from ST Microelectronics, U_6–U_8 are AD633JN multipliers from Analog Devices, all resistors R_1–R_{33} and capacitor C_1 are 0806 package with 1% accuracy and 5% accuracy, respectively. The parameter values of the circuit are directly labeled on Fig. 13(b), and the state variable x can be obtained by measuring the voltage v_x at the test point x ($v_x = 0.4x$).

The homemade OS-CCM circuit board is used to characterize the stability of the single cell, as well as the coupling-induced destabilization phenomenon in the two-cell network, as shown in Figs. 14 and 15.

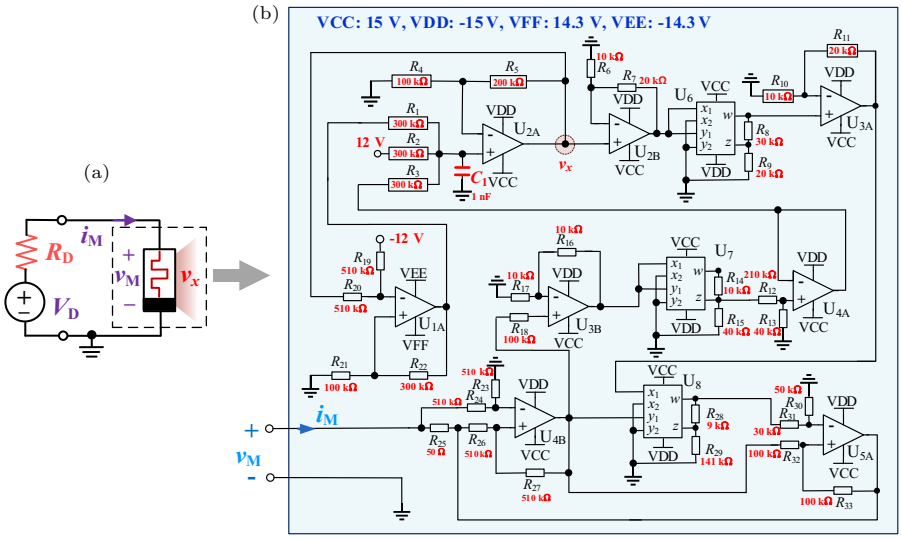


Fig. 13. Hardware implementation of the current-controlled OS-CCM. (a) Voltage-excitation configuration, where the one-port OS-CCM is biased by an ideal DC source V_D through a series resistor R_D. (b) Circuit implementation of the analog emulator built with five TL082 operational amplifiers (U_1–U_5) and three analog multipliers (U_6–U_8) that realize the memristor equations defined by Eq. (2). The surrounding resistor networks perform signal scaling, inversion, and weighted summations to interface the multiplier inputs with the port variables and internal signals. The node v_x is a test point used to observe the state variable of the memristor. VCC = +15 V, VDD = −15 V, VFF = +14.3 V, and VEE = −14.3 V are the power supply for the operational amplifiers and multipliers.

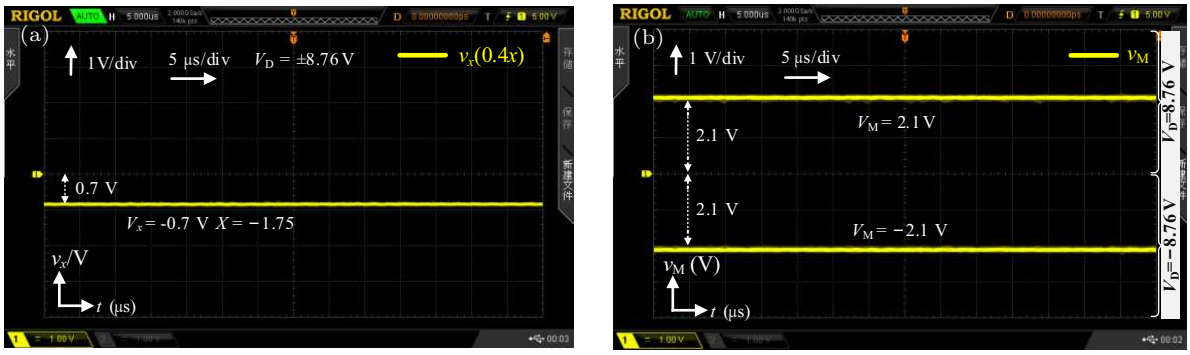


Fig. 14. Experimentally measured steady-state waveforms of a single cell made of a current-controlled OS-CCM under positive and negative bias voltages $V_D = \pm 8.76$ V. (a) Voltage waveform v_x of the single cell, corresponding to the state variable x of the OS-CCM. (b) Memristor voltage v_M of the single cell, showing two symmetrical stable states $V_M = 2.1$ V at $V_D = 8.76$ V and $V_M = -2.1$ V at $V_D = -8.76$ V.

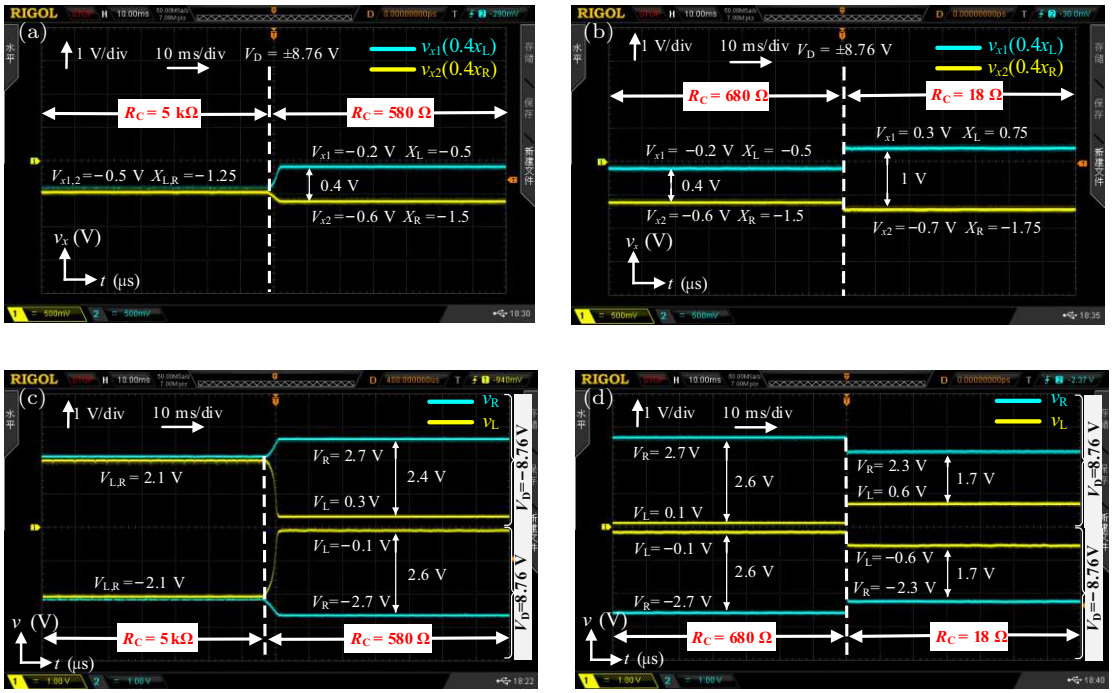


Fig. 15. Experimentally measured symmetrical Turing instability under bias voltages $V_D = \pm 8.76$ V with different coupling resistances R_C. Experimentally measured state variables x_L and x_R of the two-cell network, where two cells are stable, at $R_C = 5$ kΩ → 580 Ω in (a) and $R_C = 680$ Ω → 18 Ω in (b). Experimentally measured memristor voltages v_L and v_R at $R_C = 5$ kΩ → 580 Ω in (c) and $R_C = 680$ Ω → 18 Ω in (d). The time scale is 10 ms/div, and the gap of the stable voltage values is marked in the figure.

Figure 14 shows the experimentally measured steady-state waveforms of a single cell made of a current-controlled OS-CCM circuit board under a symmetrical bias voltage of $V_D = \pm 8.76$ V, demonstrating the stability of the left and right cells in the two-cell network. The instruments needed in the experiment are a RIGOL DS2072A digital oscilloscope and a SIGLENT SPD4323X programmable DC power supply with 4 output channels.

Figure 14(a) displays the experimentally measured voltage $v_x = 0.4x$ at $V_D = +8.76$ V, showing that v_x converges to $V_x = -0.7$ V, corresponding to the state variable x converging to $X = -1.75$. Figure 14(b) shows the experimentally measured memristor voltage v_M under positive and negative bias voltages $V_D = +8.76$ V, indicating that v_M converges to $V_M = 2.1$ V at $V_D = 8.76$ V, while it tends to $V_M = -2.1$ V at $V_D = -8.76$ V. These results indicate that the cell is stable and exhibits bistability under both positive and negative bias voltages.

Figure 15 illustrates the evolution of the experimentally measured memristor voltages $v_{L,R}$, and state variables $x_{L,R}$ for two distinct coupling resistances R_C to highlight the changes between the before and after states. Figures 15(a) and 15(b) track the voltages $v_{x1} = 0.4x_L$ and $v_{x2} = 0.4x_R$ to obtain the evolution of the state variables x_L and x_R of the two-cell network. When $R_C = 5$ kΩ, both traces settle to the same level at $V_{x1} = V_{x2} = -0.5$ V, corresponding to $X_L = X_R = -1.25$. After R_C is reduced to 580 Ω, the shared state splits into two distinct steady levels, with V_{x1} rising to −0.2 V and V_{x2} remaining at −0.6 V, corresponding to $X_L = -0.5$ and $X_R = -1.5$. Figure 15(b) illustrates that the coupling resistance R_C affects the

separation distance between the steady states of the state variables X_L and X_R. Also, the results illustrate that the evolution of the state variables of the two cells follows identical trajectories under positive and negative bias voltages.

Due to the odd-symmetrical property of the memristors in the two-cell network, unlike the evolution of the state variables x_L and x_R, the memristor voltages v_L and v_R exhibit a symmetrical destabilization phenomenon, as shown in Figs. 15(c) and 15(d). Figure 15(c) illustrates the transition of the network from its bistability to quadristability, that is, the memristor voltages v_L and v_R exhibit two stable states at $R_C = 5$ kΩ, while four stable states emerge when R_C is decreased to 580 Ω. Figure 15(d) further illustrates that the coupling resistance R_C also affects the stable states of the memristor voltages in the network. Figures 15(c) and 15(d) experimentally validate the symmetrical destabilization phenomenon under positive and negative bias voltages $V_D = \pm 8.76$ V, aka, symmetrical Turing instability. The experimental results are in quantitative agreement with the simulations in Fig. 11 within the acceptable experimental error.

This section presents the hardware implementation of the two-cell network using two homemade OS-CCM circuit boards and experimentally confirms the symmetrical Turing instability.

5. Conclusion

This paper presents a novel current-controlled odd-symmetrical CCM sibling, termed OS-CCM, and employs it to construct a two-cell network for the observation of symmetrical Turing instability. The locally active and edge-of-chaos parameter domains for the OS-CCM are rigorously analyzed using Chua's small-signal impedance analysis method, thereby demonstrating its inherent capability to induce Turing instability. When two identical current-controlled OS-CCM-based cells are coupled via a passive resistor, the originally stable states of the cells become destabilized, giving rise to two distinct stable states under positive and negative bias voltages, respectively, which demonstrates the emergence of Turing instability in a symmetrical pattern. The critical coupling resistance at which destabilization occurs is precisely identified through eigenvalue locus analysis. Furthermore, a homemade hardware circuit kit of the current-controlled OS-CCM was developed and employed to experimentally reproduce symmetrical Turing instability. Both simulation and experimental results are in excellent agreement with the theoretical analysis. This work extends the existing forms of Turing instability by introducing and rigorously validating its symmetrical pattern, and provides a theoretical foundation for the design of biphasic action potential neuron circuits, symmetrical chaotic circuits, and brain-inspired multimodal recognition and computing.

Acknowledgements

This work was supported in part by the National Natural Science Foundation of China (Grant Nos. 62501213 and 62574072), Zhejiang Provincial Natural Science Foundation of China (Grant No. LQN25F010008), and the Fundamental Research Funds for the Provincial Universities of Zhejiang (Grant No. GK249909299001-025).

References

[1] Turing A M 1952 *Philos. Trans. R. Soc. Lond. B, Biol. Sci.* **237** 37
[2] Ascoli A, Demirkol A S, Tetzlaff R and Chua L 2022 *IEEE Trans. Circuits Syst. I Reg. Pap.* **69** 4596
[3] Chua L O 2005 *Int. J. Bifurc. Chaos* **15** 3435
[4] Chua L O 2024 *Nat. Rev. Electr. Eng.* **1** 614
[5] Jin P, Ascoli A, Wang G, Liang Y, Wang X, Yuan F, Dong Y, Chen L, Iu H H C, Demirkol A S, Tetzlaff R and Chua L O 2025 *IEEE Trans. Circuits Syst. I Regul. Pap.* **73** 2015
[6] Li X, Sun J, Sun Y and Zhang J 2025 *IEEE Trans. Circuits Syst. I Reg. Pap.* **72** 8028
[7] Sun J, Li X, Sun Y, Xiong Z and He J 2026 *Chin. Phys. B* **35** 010501
[8] Xiao P D, Ma M, Jiang H Y, Huan Z, Du S and Hong Q 2026 *IEEE Trans. Ind. Inf.* **22** 969
[9] Sun J, Shen Y, Wang Y and Wang Y 2025 *IEEE Trans. Neural Netw. Learn. Syst.* **36** 11466
[10] Sun J, Gao P, Liu P and Wang Y 2025 *IEEE Trans. Ind. Inf.* **21** 5633
[11] Jiang H Y, Li T, Xiao P D, Du S and Hong Q 2026 *IEEE Trans. Circuits Syst. I Reg. Pap.* **73** 384
[12] Smale S 1976 *A Mathematical Model of Two Cells Via Turing's Equation, in The Hopf Bifurcation and Its Applications* (New York, NY: Springer New York) pp. 354–367
[13] Yan Y, Jin P, Shi J, Wang G, Liang Y, Dong Y and Chen L 2025 *Mod. Phys. Lett. B* **39** 2550042
[14] Ascoli A, Demirkol A S, Tetzlaff R and Chua L O 2022 *IEEE J. Emerg. Sel. Top. Circuits Syst.* **12** 804
[15] Leutcho G D, Gandubert G, Woodward L and Blanchard F 2025 *Chaos, Solitons Fractals* **198** 116586
[16] Wang N, Tong Y, Liu F, Li X, He Y and Fan W 2025 *Chin. Phys. B* **34** 038201
[17] Huang X X, Xiao M, Rutkowski L, Bao H B, Huang X and Cao J D 2024 *Chin. Phys. B* **33** 060202
[18] Chua L 2019 *Everything You Wish to Know About Memristors but Are Afraid to Ask, in Handbook of Memristor Networks* (Cham: Springer International Publishing) pp. 89–157
[19] Jin P, Wang G, Liang Y, Chen L, Iu H H C and Chua L O 2023 *IEEE Trans. Circuits Syst. II Express Briefs* **70** 3139
[20] Chua L O 2023 *IEEE Electron Dev. Mag.* **1** 10
[21] Kumar S, Williams R S and Wang Z 2020 *Nature* **585** 518
[22] Yi W, Tsang K K, Lam S K, Bai X, Crowell J A and Flores E A 2018 *Nat. Commun.* **9** 4661
[23] Jin P, Wang G, Liang Y, Iu H H C and Chua L O 2021 *IEEE Trans. Circuits Syst. I Reg. Pap.* **68** 4419
[24] Jin P, Wang G and Chen L 2023 *Chaos Interdiscip. J. Nonlinear Sci.* **33** 023120
[25] Li H and Min F 2025 *IEEE Trans. Circuits Syst. I Reg. Pap.* **72** 4820
[26] Chen X J, Sun K, Wang H, Liu J and Yao Z 2025 *Chaos, Solitons Fractals* **201** 117189
[27] Xu Q, Chen X J, Wu H, Iu H H C, Parastesh F and Wang N 2024 *IEEE Trans. Circuits Syst. II Express Briefs* **71** 4551
[28] Guo M, Zheng C, Dou G and Iu H H C 2026 *IEEE Trans. Circuits Syst. I Reg. Pap.* **73** 850
[29] Guo M, Zhang X W, Guo W H, Dou G, Chen D, Wang L H and Iu H H C 2026 *IEEE Trans. Circuits Syst. I Reg. Pap.* **73** 1840